Understanding copper sulfide formation from layered template and their use as power electrode materials in aqueous electrolyte

Julien Sarmet, Fabrice Leroux, Christine Taviot Gueho, Patrick Gerlach, Camille Douard, Thierry Brousse, Gwenaëlle Toussaint, Philippe Stevens

Understanding copper sulfide formation from layered template and their use as power electrode materials in aqueous electrolyte

Julien Sarmet [1], Fabrice Leroux [1*], Christine Taviot Gueho [1], Patrick Gerlach[2,3], Camille Douard[2,3], Thierry Brousse[2,3], Gwenaëlle Toussaint[3,4], Philippe Stevens[3,4]

[1] Université Clermont Auvergne, Clermont Auvergne INP, CNRS, Institut Pascal, F-63000 Clermont–Ferrand, France
[2] Nantes Université, CNRS, Institut des Matériaux de Nantes Jean Rouxel, IMN, 2 rue de la Houssinière BP32229, 44322 Nantes cedex 3, France
[3] Réseau sur le Stockage Electrochimique de l'Energie (RS2E), CNRS FR 3459, 33 rue Saint Leu, 80039 Amiens Cedex, France
[4] EDF R&D, Department LME, Avenue des Renardières, 77818 Moret-sur-Loing Cedex, France

* Corresponding author: Fabrice.leroux@uca.fr

Abstract: Copper sulfide has received increasing attention as an electrode material in past decades. In this study, we report the synthesis of copper sulfide with layered copper hydroxide salt (LHS) ($Cu_2(OH)_3NO_3$) precursors using different protocols. X-ray diffraction suggests the presence of numerous non-stoichiometric phases ($Cu_{1-x}S$) and not a pure covellite phase and SEM images show particles with flower-like shape but different in size. The solid-state kinetic parameters of the reaction refined by the JMAK method indicate a pseudomorphic transformation controlled by 1D diffusion, different in term of precursors phase, reagents and protocol applied. The microwave method needs less energy to achieve the transformation than the amine digestion (AD) method and the morphology of particles is also different. Tested in sodium acetate electrolyte, CuS provides a maximum capacity of 67 mAh/g for AD, which is much higher than for the commercial grade CuS. This is explained by the difference in nanostructuration of the flower-like shape particles obtained from the layered template. Finally, CuS is used as both a positive and negative electrode material in a complete aqueous battery system but its redox process, which is strongly diffusion limited especially in the lower potential domain, prevents the whole system from operating at high power.

Keywords: Copper sulfide; Layered Hydroxide salts; JMAK model; High-power battery

1. Introduction

A large number of research focuses today on the development of electrode materials for new high power batteries. Such fast systems could in some circumstances meet the demand for energy storage in addition to power. Open structures containing electrochemically active elements such as lamellar structures are interesting candidates as power and energy electrode materials due to a better accessibility of the redox centers and rapid diffusion in the aqueous electrolyte. Among these lamellar materials, the layered double hydroxides (LDHs) materials are at the foreground because their great versatility and tunability, making them promising for the next generation of supercapacitors (SC) and hybrid devices. [1,2]. To this end, layered double hydroxides (LDH), layered hydroxide salts (LHS) and layered oxides such as those containing nickel and cobalt cations have been widely studied and display high specific capacities [3–6]. However other materials such as nitrides of vanadium, titanium or molybdenum are highlighted for their excellent conductivity and remarkable chemical properties, conferred by their intrinsic lamellar structures associated with unique chemical bonds [7,8]. These studies have been extended to layer-structured transition-metal dichalcogenides to evaluate them as electrode material for high power energy storage devices. Indeed, various transition metal sulfides such as CoS [9], NiS [10], ZnS [11], CuS [12], Cu_2S [13], $CuCo_2S4$ [14], WS_2 [15] and CoS_2 [16] are receiving increased attention as electrode materials due to high electrochemical performance, rich and more complex valence states compared to oxides, and good chemical stability [17].

CuS, an important transition metal chalcogenide, is a typical p-type semiconductor. It is an inexpensive and abundant material with widespread applications for photocatalytic degradation [18], Li-ion batteries [19], as a catalyst for CO_2 reaction [20,21] and for solar cells [22]. As far as electrochemical storage is concerned, CuS has been evaluated as a cathode material for lithium-ion batteries as a result of its metal-like electronic conductivity (10^{-3} S/cm) and its promising redox reaction, with a theoretical specific capacity of 280 or 561 mAh/g for one or two electrons reaction, respectively [17].

Different morphologies of CuS have been obtained such as nanoplatelets [23], nanoneedles [24], nanosheets [25], nanowires [26], flower-like [27], microspheres [28] and nanospheres [23] (Table 1). For example, Huang et al. reported several morphologies using syntheses assisted with surfactants such as SDS and CTAB and for which the layered CuS provides a unique architecture for charge transport and electrolyte diffusion, giving rise to specific capacities of 38.2 and 63.2 mAh/g, respectively [25]. In addition, Raj et al. have synthesized CuS nanoplatelets using a thermal treatment, which delivered a specific capacity of 18.3 mAh/g at a scan rate of 5 mV/s with an energy and power density of 6.23 Wh/kg and 1.75 kW/kg at 3 A/g [23]. Better capacity values have been obtained with morphologies adopting nanosheet [25], flower-like [27] and nanospheres [29] that have reached specific capacities of 138.8, 215.6 and 135.7 mAh/g respectively. One aspect which is difficult to control is the morphology of lamellar CuS structure which depends on numerous parameters. Therefore, one of the most promising ways to produce the lamellar structure of sulfide materials is to use lamellar hydroxides structure precursors such as LDH or LHS as inorganic template [30,31]. For example, Nethravathi et al. have synthesized by a microwave-assisted method, 10 nm-size nanoparticles of CuS using layered hydroxysalts (LHS) intercalated with dodecyl sulfate (DS) surfactant. These were studied for sunlight photocatalysis but not yet as an electrode material [31].

Table 1. Comparison of the electrochemical performance of different morphologies of CuS reported in the literature

Precursors	**Method of preparation**	**Morphology**	**Electrolyte**	**Specific capacity (mAh/g)**	**Retention % (Cycles)**	**Ref**
$CuSO_4*5H_2O$, C_2H_5NS	LTCBD on FTO	Nanoplatelets	$LiClO_4$ (1M)	18.3	86.1 (100)	[23]
CNT@SiO_2@CuSilicat , Na_2S	Hydrothermal	Nanoneedles	KOH (2M)	16.9	100 (1000)	[24]
$CuNO_3*3H_2O$, $C_2H_6O_2$, CTAB	Solvothermal	Nanosheets	KOH (6M)	63.2	60 (500)	[25]
$CuNO_3*3H_2O$, $C_2H_6O_2$, SDS	Solvothermal	Nanosheets	KOH (6M)	38.7	62 (500)	[25]
$CuNO_3*3H_2O$, $C_2H_6O_2$, CH_4N_2S	Solvothermal	Nanosheets	KOH (6M)	138.8	75.4 (500)	[25]
Cu foil, $(NH_4)_2S_2O_8$, Na_2S	Chemical oxidation & LTCBD	Nanowires	NaOH (1M)	42.3	87 (5000)	[26]
$CuNO_3*3H_2O$, $C_2H_6O_2$, CH_4N_2S	Solvothermal	Flower-like	KOH (2M)	215.6	80 (1000)	[27]
$[Bmim]_2Cu_2Cl$, CH_4N_2S	Solvothermal	Microspheres	KOH (2M)	32.9	74 (3000)	[28]
Copolymer Pluronic P123, $Cu(Cl)_2*2H_2O$, CH_4N_2S	Solvothermal	Nanospheres	KOH (6M)	135.7	91 (2000)	[29]

* $CuSO_4*5H_2O$: Copper sulfate pentahydrate, C_2H_5NS : Thioacetamide, LTCBD : low temperature chemical bath deposition , FTO : Fluorine-Doped Tin Oxide, $CuNO_3*3H_2O$: Copper nitrate trihydrate, $C_2H_6O_2$: Ethylene glycol , CH_4N_2S : Thiourea, CTAB : Cetyltrimethylammonium bromide, $(NH_4)_2S_2O_8$: Ammonium persulfate, CC : Carbon cloth, CNT : Carbon Nanotubes, $[Bmim]_2Cu_2Cl$:1-Butyl-3-methylimidazolium copper chloride, $Cu(Cl)_2*2H_2O$: Copper chloride dihydrate

The material undergoes a large change in volume due to strong structural distortions making its cycling response unstable. Hence, it is necessary to control the CuS morphology and combine the material with electronically conductive carbon or carbonized by-product to enhance electric contact and the performance greatly [29,32] (Table 2). For example, composites with carbon and copper sulfide such as carbonized carbon cloth, reduced graphene oxide or multi-walled carbon nanotubes exhibit a specific capacity of 779.3, 386.3 and 471.8 mAh/g, respectively [37,39,25]

Table 2. Comparison of CuS composites and its derivatives described in the literature

Composite	**Precursors**	**Method of preparation**	**Morphology**	**Electrolyte**	**Specific capacity (mAh/g)**	**Retention % (cycles)**	**Ref**
CuS/3D graphene	$CuNO_3*3H_2O$, C_2H_5NS	LTCBD	Flower-like	KOH (3M)	41.5	95 (5000)	[32]
CuS/GO	$Cu(CH_3COO)_2*H_2O$, CH_4N_2S	Hydrothermal	Nanosized particles	KOH (3M)	38.2	70 (5000)	[33]
CuS/rGO	$Cu(Cl)_2*2H_2O$, CH_4N_2S	Solvothermal	Polygon on rGO nanosheet	KOH (6M)	262.8	89 (5000)	[34]
CuS/rGO	$Cu(Cl)_2*2H_2O$, CH_4N_2S	Hydrothermal	Hexagonal	KOH (3M)	22.8	97 (5000)	[35]
CuS/GO nanosheet	$Cu(CH_3COO)_2*H_2O$, CH_4N_2S	Solvothermal	Nanoplatelets	KOH (6M)	83.0	80 (2000)	[36]
CuS/MCC	$CuNO_3*3H_2O$, CH_4N_2S	Electrodeposition	Nanosheet	PVA-KOH	779.3	89.8 (10000)	[37]
CuS-CC	$CuSO_4*5H_2O$, C_2H_5NS	Solvothermal	Nanoflake	KOH (3M)	59.3	75.1 (5000)	[38]
Hollow-CuS/rGo	$CuNO_3*3H_2O$, CH_4N_2S	Solvothermal	Hollow spheres	KOH (6M)	386.3	96.2 (1200)	[39]
CuS/PPy	$CuNO_3*3H_2O$, CH_4N_2S	Solvothermal	Sphere-like	KCl (1M)	118.6	88 (1000)	[40]
CuS/MWCNT	$CuNO_3*3H_2O$, CH_4N_2S	Solvothermal	Layered platelets	KOH (6M)	471.8	90 (600)	[25]

*MWCNT : Multi-walled Carbon Nanotubes, PPy: Polypyrrole, GO: Graphene Oxide, rGO: reduced Graphene Oxide, CC: Carbon Cloth, CH_4N_2S; Thiourea, $CuNO_3*3H_2O$: Copper nitrate trihydrate, $Cu(CH_3COO)_2*H_2O$: Copper acetate monohydrate, $CuSO_4*5H_2O$: Copper sulfate pentahydrate, C_2H_5NS : Thioacetamide , $Cu(Cl)_2*2H_2O$: Copper chloride dihydrate , MCC : Mesoporous carbonized clothes

As previously indicated, numerous synthesis protocols have already been used to synthesize the CuS phase. However, synthesis of the pure phase is not straightforward, and a mixture of CuS/Cu_2S phase is the most commonly obtained product. This study reports the results obtained only for ~~pure~~ phases containing crystallized CuS, together with the formation mechanisms. The main goal is to use copper – LHS nitrate or the DS intercalated compound as a template to control CuS particle morphology. The operating protocol was compared to other synthesis methods, currently used for the

synthesis of CuS from metal salts, which we have adapted for the transformation of the copper-LHS template. First, the solid-state phase formation kinetics for each protocol were studied by combining X-ray diffraction (XRD) and scanning electron microscopy (SEM) and using the JMAK (Johnson–Mehl–Avrami–Kolmogorov) theory. Kinetic parameters, such as activation energy, could be compared between protocols. In the second part, the electrochemical behaviour was investigated by cycling voltammetry.

2. Materials and methods

2.1. Synthesis of $Cu_2(OH)_3(NO_3)$ and $Cu_2(OH)_3(DS)$ precursors

For the synthesis of $Cu_2(OH)_3(NO_3)$ samples, AR grade raw chemicals were used. Copper oxide (CuO, 98%), copper nitrate trihydrate ($Cu(NO_3)_2*3H_2O$, 98%), sodium dodecylsufate (DS, >90%) were purchased from Aldrich, sodium hydroxide (NaOH, 98%).

15.9 g of CuO (0.2 mol) were dispersed into 200 mL of a 1.25 mol/L aqueous copper nitrate solution. The mixture was stirred for 4 weeks under a nitrogen atmosphere after which the solid was recovered by centrifugation at 4500 rpm (relative centrifugal force of 3056xg), washed three times with deionized water and dried at 60°C in oven.

About 100 mg of the $Cu(OH)_3(NO_3)$ was dispersed in 4-5 mL of the aqueous solution of doecylsulfate (DS) (concentration about 0.1 M) and allowed to react for 2 days at 65 °C. The supernatant solution was centrifuged, and the solid material was again reacted with a fresh salt solution for 2 days at 65 °C. The organic derivatives were washed three times with water and dried at 60°C in the oven.

2.2. Synthesis of CuS

For the synthesis of CuS using the amine digestion (AD) method, AR grade raw chemicals were used. Triethanolamine (TEA,99.5%) and isopropanol (IPA,99%) were purchased from Aldrich. AD is inspired by Pejjai et al. protocol [30]. 0.025 mol of $Cu(OH)_3(NO_3)$ was dissolved with vigorous stirring in 50mL od deionized water during 20 min. 1 mL of triethanolamine (TEA), and 2 mL of isopropyl alcohol (IPA) were added and stirred vigorously for 30 min at 70°C or 90°C. Next a 150 mL of an aqueous solution with 0.053 mol (1:2) of thiourea were added and the pH was adjusted at 10 by adding NaOH. The mixture was allowed to react for 30min at constant temperature controlled by a thermostatic bath Julabo-F12. The precipitate was collected and centrifuged at 4500 rpm for 5 minutes and washed three times with water and ethanol and dried at 60°C overnight.

For the synthesis of CuS using microwaves, AR grade raw chemicals were used. 1-butanol (99%) and thiourea (99%) were purchased from Aldrich. The microwave method was inspired by the. protocol of Nethravathi et al [31]. Copper hydroxyl dodecylsulfate or nitrate (0.2g) were put in suspension into 80 mL of 1-butanol by sonication for 1h at room temperature. Thiourea (0.1g) was added and the mixture was sonicated 5 minutes. The resulting mixture was then poured into 80 mL vessels and irradiated with microwaves at a power of 300 W using a Discover® SP-D 80 microwave for different periods of time and different temperatures; the pressure reached was around 290 psi. The black precipitated was isolated by centrifugation, washed with a mixture of water and ethanol (1:1; v:v) and dried in the oven at 60°C.

2.3. Electrode preparation

In order to evaluate the electrochemical performance of the composite, the CuS prepared (active matter) was incorporated into an electrode using a typical self-supporting electrode process. To do so, the active material, an electronically conductive additive (carbon black, Superior Graphite Co., >99%) and a polymer binder (PTFE, 10 %wt. in solution in water) were mixed in 15 mL of ethanol so as to have 60, 30 and 10 % by mass of each component respectively. The mixture was then stirred and heated to 60-70°C to partially evaporate the solvent and obtain a homogeneous paste. The paste was then cold rolled to produce a sheet of approximately 150 µm thickness, before being dried in an oven at 60°C overnight. Electrodes with a diameter of 10 mm were then cut from the paste and pressed into a stainless steel grid current collector (316 L, 0.160 mm, Saulas) for 1 minute at 5 tons. The total mass loading of the electrode composite material was between 5 to 10 mg/cm².

2.4. Reagents and chemicals

For the LSH synthesis, copper nitrate trihydrate was purchased from Merck (≥99%, Saint-Quentin-Fallavier Cedex, France) and sodium dodecylsufate was from Acros (≥99%, Geel, Belgium). Copper Sulfide (CuS) was from Merck (≥99%, Saint-Quentin-Fallavier Cedex, France)

For electrode preparation, carbon black (SG, >99%, Superior Graphite Co., Sundsvall, Sweden) and polytetrafluoroethylene (PTFE, 60 wt% in water, Merck, Saint-Quentin-Fallavier Cedex, France) were used.

For electrochemical experiments sodium acetate (CH_3COONa, ≥99%, Merck, Saint-Quentin-Fallavier Cedex, France) was used. Deionized water was employed for all experiments.

2.5. Analysis

X-ray diffraction analyses were performed using a theta−theta PANalytical X'Pert Pro diffractometer equipped with a Cu anticathode (λKα1 = 1.540598 Å, λKα2 = 1.544426 Å) and an X'Celeretor detector. For the phase identification and refinement of the unit cell parameters of the series of samples, the X-ray patterns were recorded in the Bragg-Brentano geometry in the range of 2−80°/2θ with a step size of 0.325°/min three times.

Scanning electron microscopy (SEM) images were recorded using a JSM-7500F field-emission scanning electron microscope operating at an acceleration voltage of 3 kV and magnifications of ×1K, x10K and×20K. Samples to be imaged were mounted on conductive carbon adhesive tabs and coated with a gold thin layer.

Surface areas were determined from the BET analysis of nitrogen adsorption isotherms recorded at 77 K using a Micromeritics ASAP 2020.

Cyclic voltammetry (CV) curves were performed using a Biologic VMP3 with a three electrodes setup with LDH/SG/PTFE as a working electrode, Ag/AgCl (KCl sat) as a reference and platinum as a counter electrode. The aqueous electrolyte salt was sodium acetate.

3. Results and discussions

3.1. Synthesis of precursors phases

In a previous work [41], we synthesized copper hydroxynitrate phase by the salt-oxide method. This method was based on the hydrolysis of divalent metal salts in the presence of metal oxide. In the present case, the reaction was conducted over four weeks and micron size particles were obtained with a coarse rod-like shape indicating a directed aggregation of primary platelet crystals in the stacking direction (Fig. 1a). The high purity and crystallinity of the sample enabled a Rietveld refinement of the XRD data and showed a structure similar to the Rouaite mineral (LSHCu-NO_3). Intercalation of dodecyl benzenesulfonate (LSHCu-DS) was also performed. As expected, the positions of the basal reflections are shifted to lower 2θ values, i.e. higher d value, indicating an expansion in the interlayer distance (Fig. 1b). The intercalated sample shows a distinct reflection at d = 2.61 nm and SEM images show deagglomeration of LSHCu particles.

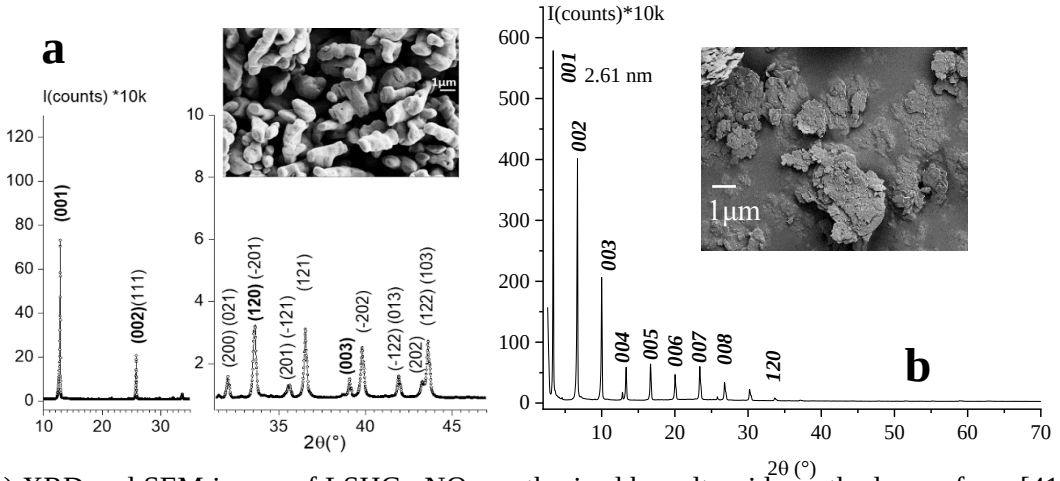

Figure 1. (a) XRD and SEM image of LSHCu-NO_3 synthesized by salt-oxide method copy from [41] and (b) XRD and SEM image of LSHCu-DS of LSHCu-DS

3.2. Synthesis of CuS phase

Two protocols were used to synthesize ~~pure~~ CuS particles. A first protocol is based on the reaction between LSHCu-NO_3, thioetylonamine (TEA) and thiourea while a second was carried out using LSHCu-NO_3 (MW-NO_3) or LSHCu-DS (MW-DS) with thiourea irradiated by microwaves (MW). Figure 2 shows the XRD patterns of copper sulfide powders when the temperature of reaction for AD was set from room temperature up to 90°C with a molar ratio Cu/S of 1:2. For MW, the microwave protocol, the temperature ranges from 80°C up to 150°C.

After reaction using either AD or MW protocol, the XRD recorded are compared to the synthetic covellite CuS (Fig. 2). This chalcogenide crystallizes with a hexagonal structure in the space group P63/mmc with the lattice parameters a = 3.77 Å and c = 16.42 Å. Most of the diffraction peaks coincide with covellite (CuS), *i.e.* 2θ = 27.6, 29.2, 32.1, 47.9, 52.7 and 59.3° as reported for ~~the Miller indices~~ *101*, *102*, *103*, *110*, *108* and *116* reflections, respectively [42]. This figure indicates no significant differences on the main diffraction peaks in the 2-theta axis, however the intensity of some peaks vary as a function of the temperature for the same reaction time. Based on the stacked XRDs, most of the diffraction peaks at the higher temperature of 90°C match those of covellite. However, for all the syntheses, the intensity ratios between the peaks do not correspond exactly to covellite. This result suggests that several $Cu_{1-x}S$ phases are present here. Studies have shown the possibility of obtaining numerous non-stoichiometric phases whose DRX signatures looks like CuS and CHNS analysis (Table S1) gives a bulk composition comprising between $Cu_{1.28}S$ et $Cu_{1.38}S$ [43]. The temperature is important for the layered pristine inorganic phase to fully react and yield crystallized CuS. For AD, the crystallinity of CuS is largely improved with temperature, a longer reaction time also increases its crystallinity (Fig. S1). For MW-DS, a temperature of 80°C is sufficient to obtained ~~pure~~ CuS. After a reaction at 100°C, the intensity of diffraction peaks of CuS increase. As is the case for AD, the temperature and the reaction time increase the crystallinity of the synthesized phases (Fig. S2). However, for MW, there is a striking difference between the two pristine phases. After 1 h at 150°C of microwave irradiation, a mixture between LSH-NO_3 starting phase and CuS is obtained, underlining that the reaction is not complete in the temperature range used. It also underlines the fact that the microwave irradiation is more efficient for more open structure such as surfactant interleaved LSH than for a compact layered assembly composed of intercalated nitrate anions. To obtain a ~~pure~~ CuS phase, it is necessary to apply a temperature of 150 °C for at least 120 minutes (Fig. S3).

For the two reactions yielding CuS, SEM images show nanoplatelets with a flower-like shape and a size of the particles dependent of the temperature and synthesis time (Fig. 3 and S4). The conservation of the initial lamellar shape suggests a "soft" structural transformation of pseudo topochemical type [44]. Pseudo topochemical transformation is well known for solid-state transformation, especially to produce micelle-templated silicas (MTS) like MCM-41 amorphous starting from silica particles with the same morphology, using an alkaline solution to dissolve the silica and reprecipitate it around surfactant micelles to yield ordered MTS structures [45] . This type of transformation has also been used for the synthesis of zeolites [46], layered double hydroxides [47] or $FePO_4$ [48]. In comparison to AD, the particles obtained by MW are smaller which is also shown by the relative intensity of the diffraction peaks between both processes (Fig. 3). This is caused by the different supersaturation conditions (concentration of dissolved species, ie. the dissolution of the LSHCu template). In high supersaturation conditions, crystal nucleation dominates crystal growth, leading to the appearance of smaller crystals. These results have led us to compare the formation mechanisms between both operating protocols.

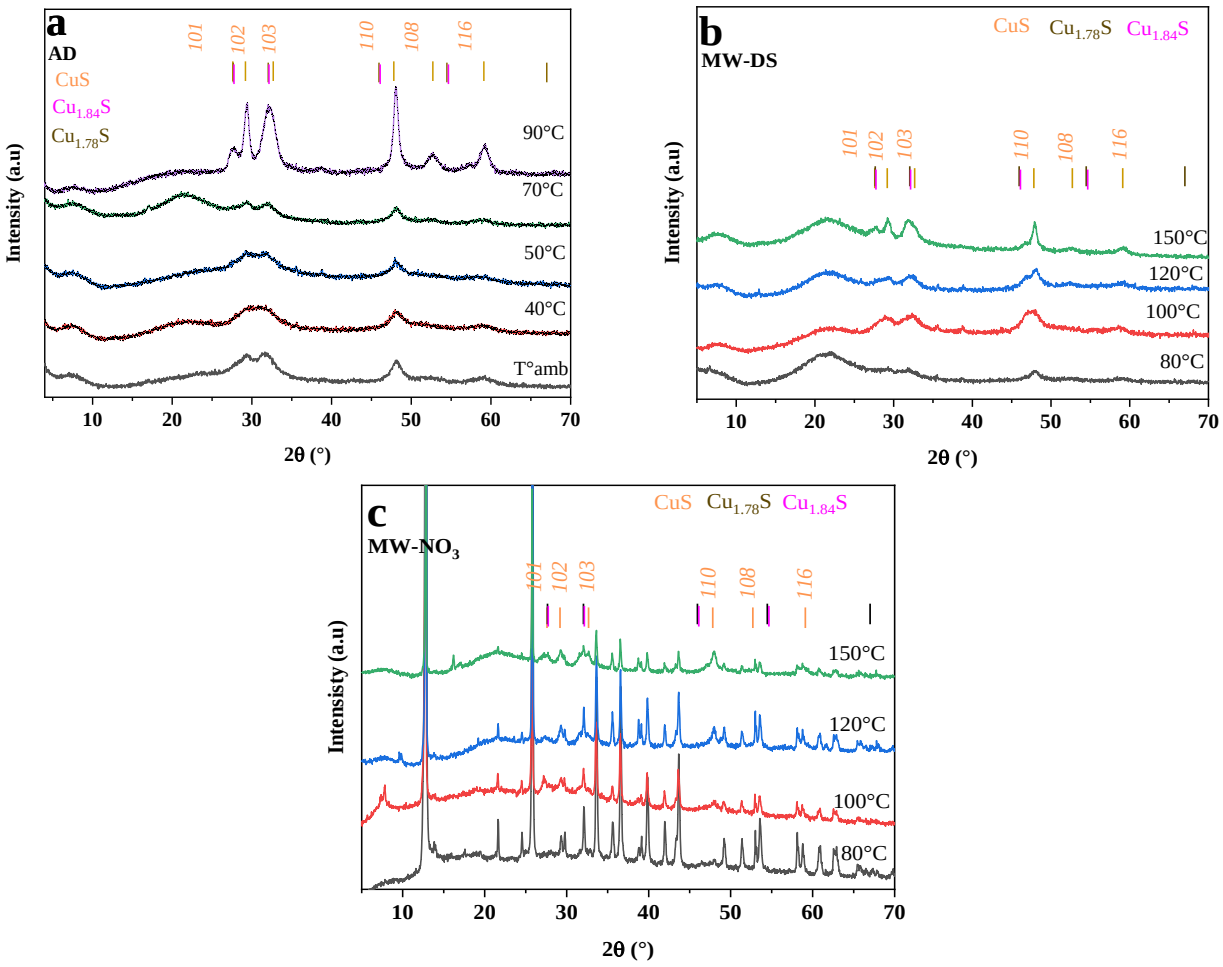

Figure 2. XRD after reaction using (a) AD after 4 h from LSH-NO_3 (b) MW-from LSH-NO_3 after 1 h and (c) MW from LSH-DS after 1 h. The temperature of reaction is indicated. Vertical orange lines correspond to covellite CuS, pink lines to $Cu_{1.84}S$ and brown lines $Cu_{1.78}S$.

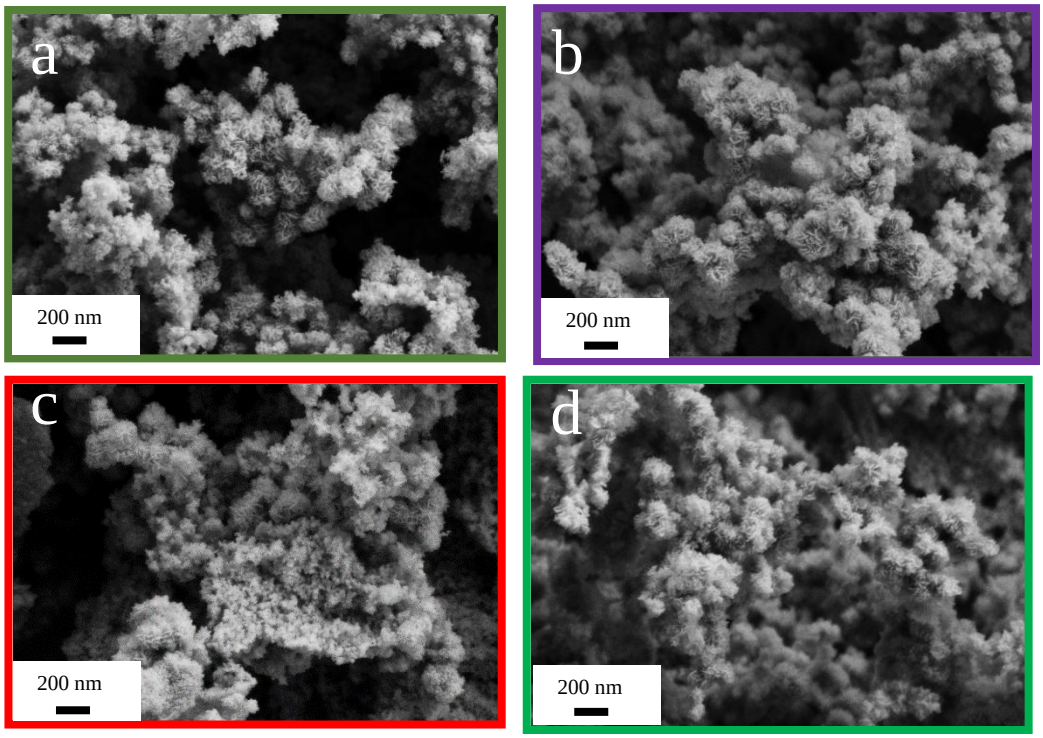

Figure 3. (a) SEM images of AD-70°C-1H and (b) SEM images of AD-90°C-1H, (c) SEM image of MW-DS-150°C-30min and (d) SEM image of MW-DS-150°C-1H

3.3. Analysis of the associated structural transformation

In order to follow the conversion process between LSH and CuS, classical models interpreting the solid state kinetics were considered based on nucleation and nuclei growth models (*i.e.* ingestion or coalescence), dimension-dependent diffusive models, dissolution/ precipitation or simple order-based models when the rate depends on the concentration or remaining fractions of reactants [49]. Models of solid-state kinetics are known to be well adapted to processes involved in the structural transformation of layered inorganic templates like LDH or LSH phases [50,51].

By measuring the change in intensity of diffraction peaks between CuS *110* and LSHCu-NO_3 or LSHCu-DS templates *120* (Fig. 4), it is possible to follow the structural transformation. Experimentally, the fraction of LSH converted to CuS (α_{CuS}) at a given time was estimated from the associated peak area ratio from their diffraction line refined by Thompson–Cox–Hastings (TCH) pseudo-Voigt and by choosing the in-plane contribution *110* for CuS and *120* for the templates.

The progress of the reaction between the two phases crosses at the value of 0.5 (Fig. S5) for all the protocols, which proves that the transformation takes place without a reactionary intermediate. The intersection between the curves differs in time according to the protocols and the phases used. For amine digestion method (AD) less than one minute is required to reach 50 % conversion at 22°C. By increasing the temperature to 70°C and 90°C, it is almost instantaneous. To study the conversion mechanism, it is therefore necessary to lower the temperature using a refrigerated thermostatic bath to have access to longer conversion times. A similar finding was observed for MW-DS for which temperatures of 120°C and 150°C led to a spontaneous reaction (< 3 min for 50 % conversion). A lower temperature of 80°C makes it possible to reduce the 50 % conversion time to 20 minutes. These results indicate that 1) the transformation is strongly temperature dependent, 2) the template impacts the conversion rate. Indeed, for the microwave treatment (MW) and using the same temperature of 150°C, half an hour is needed for the NO_3 template to be 50 % transformed (and 2 hours for complete transformation) while it only takes 1 minute (5 minutes to completion) for the DS LSH template. At 80°C, the conversion times are even more different.

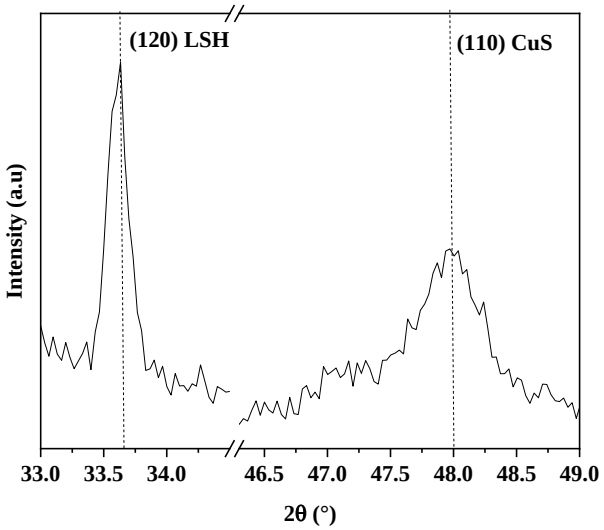

Figure 4. Selected in-plane diffraction peak for LSH *120* and CuS *110* to calculate α_{CuS} applying the JMAK refinement.

The progress of reaction exemplified by the function $\alpha_{CuS} = f(t)$ is modeled by a general growth mechanism using Johnson–Mhel–Avrami–Kolmogorov's (JMAK) equation:

$$\alpha_{CuS} = 1 - \exp(-k(t-t_0)^n) \quad (1)$$

in which k is an effective rate constant and n the Avrami exponent related to the kinetic model and t_0 the induction time (Fig. S6). The Avrami number n is obtained by plotting and fitting $\ln(-\ln(1-\alpha_{CuS})) = f(t-t_0)$ by a straight line. The determination of the kinetic parameters k then enables the activation energy E_a to be obtained according to the Arrhenius equation:

$$k = A.\exp(-E_a/RT) \quad (2)$$

where k, E_a, A, R and T correspond to the rate constant, the activation energy ($kJ.mol^{-1}$), the pre-exponential factor, the perfect gas constant ($R = 8.314\ J.mol^{-1}.K^{-1}$) and the temperature (in K), respectively.

The fitted Avrami number (n) for all the syntheses and temperatures are presented in Table 3. Most values of n are below 1, thus deviating from the expected value of 1 for a layered system; which indicates a complex process controlled by diffusion [52]. The Avrami number depends on dimensionality of growth and on whether nucleation is instantaneous or sporadic. In this case the interpretation of the growth model deduced from the Avrami number is an instantaneous nucleation with needle-like growth [53]. The kinetic parameter k, determined by applying the JMAK model, increases as a function of the temperature and is found to be dependent of the initial template. As expected from the progress of the reaction which is different between both templates when using MW, the kinetic parameter is also very dependent on the temperature. Interestingly, much higher k values for DS LSH are obtained than for the nitrate template, but it leads to equal activation energies, since the slopes of the fitted lines are parallel (Fig. 5d): an activation energy to convert LSH platelets to CuS of 70 kJ/mol is observed for both DS and NO_3 templates. However, for AD and from the same NO_3 LSH template, the activation energy is 250 kJ/mol, four times higher than that found for the MW method. The decrease in the activation energy using MW was also reported for the rapid synthesis of cubic particles of cuprous oxide [54]. As a comparison, layered templates have an activation energy of 27 kJ/mol for the diffusion of Li into γ-gibbsite [55] and 145 kJ/mol is needed to convert LSH zinc to LDH ZnAl in presence of PES polymer and Al(hydroxyl)acetate [50].

It clearly appears that the microwave treatment (MW) reduces the synthesis time as well as the activation energy required for the reaction to occur. Under the electromagnetic field generated by microwaves, it is known that the molecules collide, generating hot spots that accelerate the reaction kinetics [41]. Having in mind that the microwave treatment requires the same energy to thermally activate the reaction, the data obtained for the kinetic parameters may seem puzzling (Fig. 5b and c):

they could be explained by the term A which represents the ordinate at the origin and which is the pre-exponential factor of the Arrhenius equation. The usual assumption is that this factor A is independent of the temperature and in the transition state theory, i.e. Eyring equation, that contains a term of entropy of activation while the activation of energy E_a is related to the enthalpy (Eq.3) [54].

$$ln\left(\frac{k}{T}\right) = \left(ln\frac{k_B}{h} + \frac{\Delta S^+}{R}\right) - \left(\frac{\Delta H^+}{R}\right)\frac{1}{T} \quad \#(3)$$

where k, k_b, ΔS^+, ΔH^+, h, R and T correspond to the rate constant, the Boltzmann constant (k_b = 1,381 × 10^{-23} $m^2.kg.s^{-2}.K^{-1}$), the entropy of activation (in $J.mol^{-1}$), the enthalpy of activation (in $J.mol^{-1}$), the Planck's constant (h = 6,626 × 10^{-34} $m^2.kg.s^{-1}$), the perfect gas constant (R = 8.314 $J.mol^{-1}.K^{-1}$) and the temperature (in K), respectively.

The simple comparison in ln(k) indicates a more important change of entropy for DS LSH than for the NO_3 template, that may be interpreted by greater disorder in the former case more favorable for the transformation to take place. Regarding the template, DS LSH offers more possibility than NO_3 LSH for species to diffuse and react with its much larger interlamellar space, thus decreasing the ignition time for the transformation to occur, in agreement with the observation (Fig. 4 b and c), while the energy (enthalpy of activation) to do so is the same for both templates. In addition, the nature of the reagents also plays a key role in the activation energy values. Copper complexation increases the energy barrier and therefore the E_a. The AD method, uses two complexing agents (TEA and thiourea) and therefore a higher E_a than the MW method (which uses thiourea alone) is needed to remove the complex and react with the sulfur.

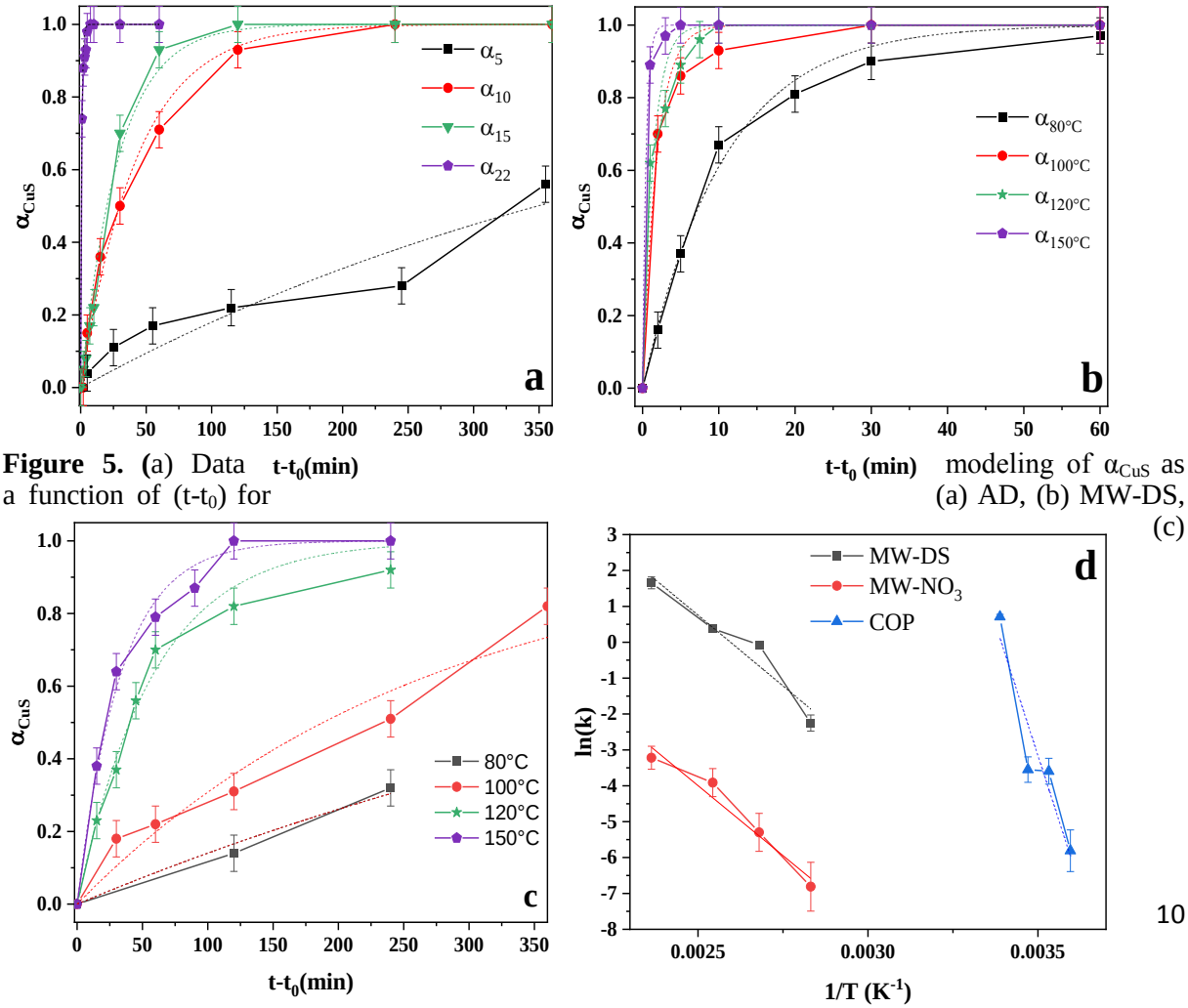

Figure 5. (a) Data t-t$_0$(min) a function of (t-t$_0$) for modeling of α_{CuS} as (a) AD, (b) MW-DS, (c)

MW-NO_3 at different temperatures using JMAK refinement (± 10% value error bars are estimated) and (d) Arrhenius plot of ln k *vs*. 1/T for diffusion model determined by using the JMAK model (± 10% value error bars are estimated

SEM images confirm a pseudomorphic type behaviour of the transformation between the two compounds (Fig.6 and S7). For the AD protocol, the agglomerated platelets of the template are first separated, then particles grow on their surface. The particles have a round shape with a relatively homogeneous size distribution of about 50 nm. By zooming in, we see that these nanosized spheres are composed of leaves, the whole resembling mimosa flowers (Fig.6a). For MW protocols, butanol medium is known to exfoliate layered hydroxides structure to single platelets [56-58]. The exfoliation process is aided by the presence of DS in the interlamellar space, which explains why the reaction is faster for the phases intercalated with DS. For MW-DS, CuS particles appear in only 5 minutes, their size increases with synthesis time, leading to nanosized platelets with a nano-flower like structure (Fig.S7). We note differences in morphologies and progress of the reaction by changing the template during MW. For example, 30 minutes are needed to obtain CuS from the nitrate phase, in accordance with the monitoring of the evolution by DRX. The size of the primary platelets, although still nanometric, is larger however than those of the other protocols, they agglomerate together to form micron-sized aggregates (Fig. 6b).

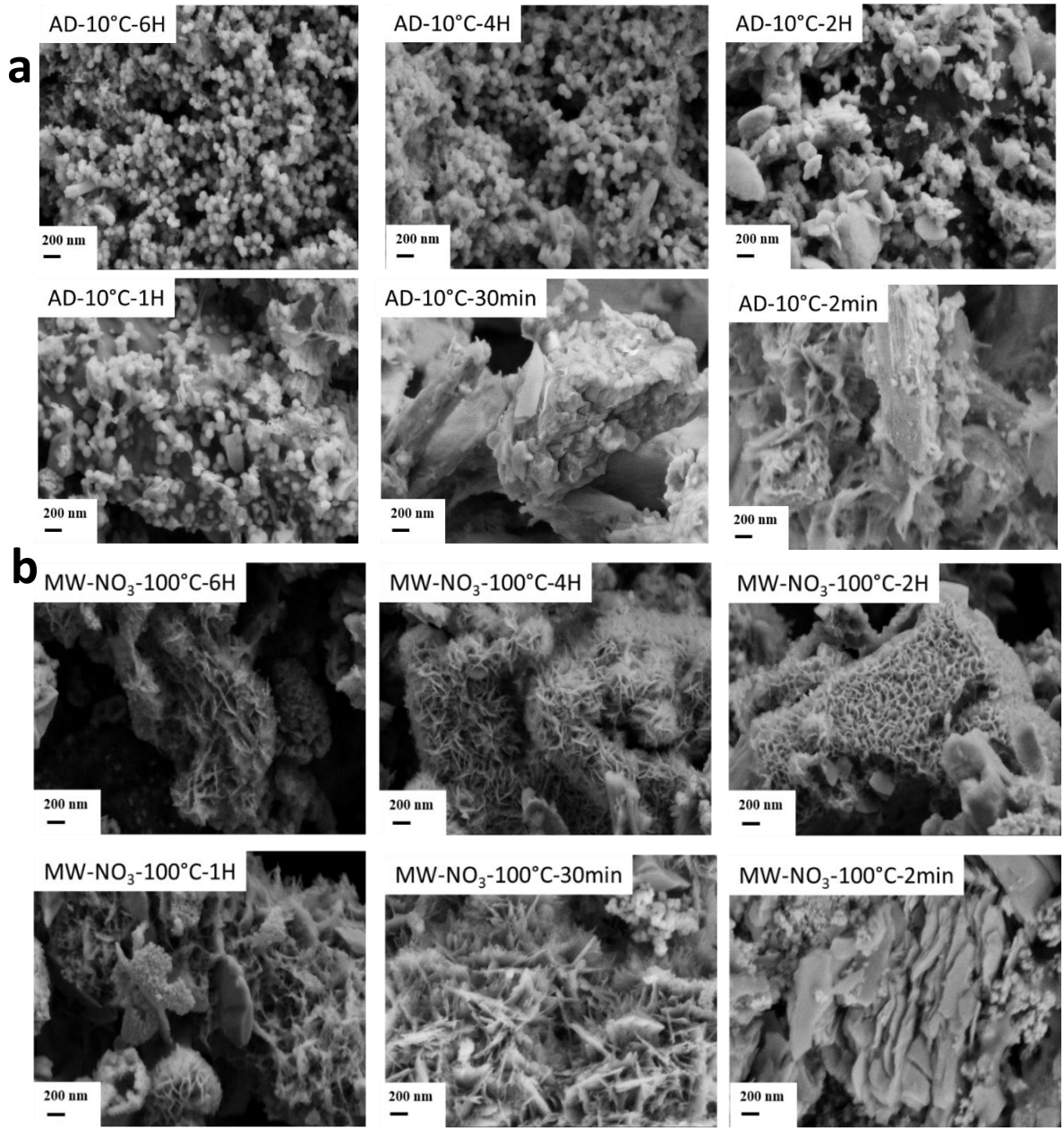

Figure 6. SEM images of (a) AD-10°C and (b) MW-NO_3 at different synthesis times

Table 3. Comparison of refinement JMAK parameters and activation energy

Protocols	*Temperature*	**n**	**k**	**Activation Energy (kJ/mol)**
AD	**5°C**	*0.7*	*0.003*	*250 ± 50*
	10°C	*0.9*	*0.027*	
	15°C	*1.2*	*0.028*	
	22°C	*0.6*	*2.03*	
MW-DS	**80°C**	*0.9*	*0.11*	*70 ± 10*
	100°C	*0.5*	*0.93*	
	120°C	*0.6*	*1.47*	
	150°C	*0.4*	*5.23*	
MW-NO_3	**80°C**	*1.4*	*0.001*	*70 ± 10*
	100°C	*0.9*	*0.005*	
	120°C	*0.8*	*0.02*	
	150°C	*0.8*	*0.04*	

3.4. Electrochemical behavior

As a reminder, CuS is composed of $Cu^{+}_{x}Cu^{2+}_{(1-x)}S^{-}_{x}S^{2-}_{(1-x)}$ with x = 2/3 : it is therefore possible to oxidize Cu^{+} to Cu^{2+} when first sweeping the potential to more oxidative values or to reduce Cu^{+} in Cu^{0} when starting first at lower potential as follows (adopting a cation redox for the two electrochemical reactions):

$$Cu_x^+ Cu_{(1-x)}^{2+} S_x^- S_{(1-x)}^{2-} - ye^- + yA^- \rightarrow A_y Cu_{(x-y)}^+ Cu_{(1-x+y)}^{2+} S_x^- S_{(1-x)}^{2-}$$

$$Cu_x^+ Cu_{(1-x)}^{2+} S_x^- S_{(1-x)}^{2-} + ze^- + zC^+ \rightarrow C_z Cu_z^0 Cu_{(x-z)}^+ Cu_{(1-x)}^{2+} S_x^- S_{(1-x)}^{2-}$$

The theoretical capacity of Cu^{+} in CuS in oxidation, ie. Cu^{+} to Cu^{2+} is 187 mAh/g, *i.e.* when y = x and the theoretical capacity of Cu^{+} in CuS in reduction, ie. the total amount of Cu^{+} to Cu^{0} is the same, *i.e.* when z = x

One cannot discard the possibility of reduction of Cu^{2+} right down to Cu^{0}, unless these two electrochemical processes are separated as it will be shown in a symmetric display using CuS at both electrodes. Considering the two electrochemical reactions, the coulombic charge between the first oxidation and the first reduction corresponds to the Cu^{+} initial content within CuS.

When first starting with an oxidative CV sweep of CuS, a fast faradic-like behaviour is observed in the potential range between -0.2 to 0.8 V (*vs*. Ag/AgCl), but with a relatively low coulombic efficiency, as shown by the pronounced difference in intensity between the oxidation and reduction wave. This is regardless of the protocol used. The CVs presented in Figure 7a,b and S8 indicate that the reaction is largely irreversible during the first oxidation since such large intensity is not recovered after the first cycle. This may be explained by either a possible degradation of the active matter and be related to an oxygen evolution reaction. After three cycles, the CVs are stabilized and the redox waves of Cu(II) to Cu(I) are located at 0.05 V and 0.30 V (*vs*. Ag/AgCl) in reduction and oxidation, respectively. Capacity values recorded in the third cycle after stabilization are 66 mAh/g for both materials prepared by AD and MW-DS-120°C-30min. This value represents only 35% of the theoretical capacity, indicating a degradation of the material during the first two cycles.

Better capacities seem to be obtained for the particles with a higher specific area (> 20 m²/g). For the MW-DS protocol characterised by SEM and XRD (see above), smaller particles are formed (~~which are less crystallized~~), the capacities after the 3rd cycle are higher. This difference of capacity could also be the result of the not pure CuS phase synthesized and the different ratios between the non-stoichiometrics phases of the materials obtained (not determined in this study).

Such a trend is also observed for the commercial product that is composed of large and well crystallized particles as shown by SEM images and XRD (Fig.S10), but it reaches a capacity of 9 mAh/g after three cycles. Even if gas adsorption analyses (BET) show limited porosities for most of the samples, a clear difference is observed in terms of specific surface area (Fig.S11). The samples synthesised by the lamellar template exhibit specific surface areas ranging from 10 to 20 m²/g, much larger than the commercial CuS. It underlines the beneficial effect of nanostructuration on the electrochemical active sites, more exposed and thus giving rise to superior electrochemical performances as usually observed in the literature [59].

Indeed, this nanostructuration is not acting on the particle surface only. Interestingly, by varying the scan rate and plotting the evolution of the capacity, it is possible to distinguish between electrochemical processes occurring purely at the surface and those that are diffusion-limited. Experimentally, the Q/Q_{max} ratio are reported using Q_{max} with the slower sweep rate of 0.5 $mV.s^{-1}$ and it shows a pronounced decrease in capacity when increasing the scan rate since at fast scan rates (5 $mV.s^{-1}$), less than 60% of Q_{max} was reached (Fig. 7d). It underlines that the redox reaction is not occurring at the particles surface only but also involves diffusion inside the particles.

For all the syntheses, the capacity is rapidly fading (Fig. 7c and S8) and the loss of capacity is only due to the transformation of the starting material, as shown by the SEM-EDX images which prove the integrity of the carbon and PTFE additives (Fig. S9).

Table 4. Results of CV experiments of AD and MW-DS at 2 mV/s in sodium acetate (1M) in [-0.2; 0.8] V.

	Q_{charge} (mAh/g) 3rd cycle*	$Q_{discharge}$ (mAh/g) 3rd cycle*	C. Efficiency (%)	Q_{charge} (mAh/g) 20th cycle*	$Q_{discharge}$ (mAh/g) 20th cycle*	C.Efficiency (%)	S_{BET} (m^2/g)
AD-70°C-1H	*67*	*34*	*51*	*13*	*10*	*77*	*25*
AD-90°C-1H-	*66*	*31*	*47*	*9*	*7*	*78*	*26*
MW-DS-120°C-30min	*66*	*32*	*48*	*8*	*7*	*88*	*19*
MW-DS-120°C-60min	*39*	*27*	*70*	*10*	*9*	*90*	*12*
MW-DS-150°C-30min	*45*	*26*	*58*	*8*	*6*	*75*	*13*
MW-DS-150°C-60min	*51*	*25*	*49*	*7*	*6*	*85*	*12*
CuS-CG	*9*	*7*	*78*	*2*	*1*	*50*	*< 1*

* Capacity and columbic efficiency include all the possible parasitic reactions taking place during the cyclic voltammetry tests

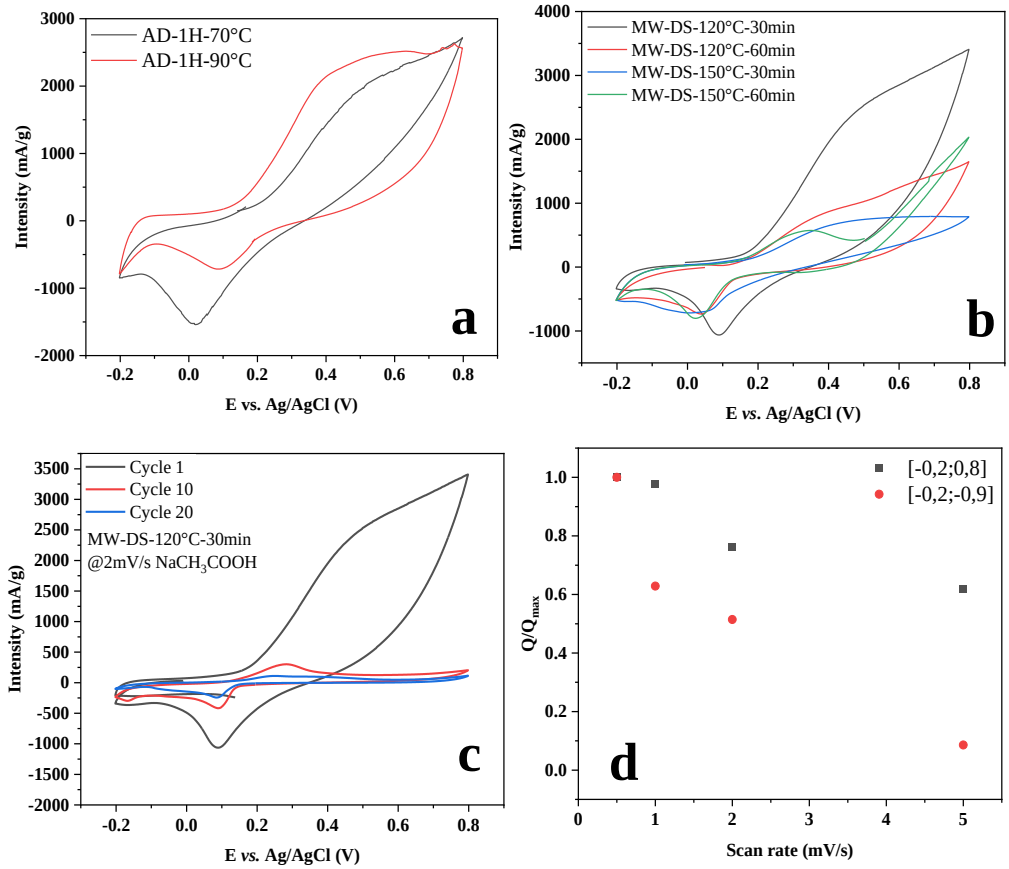

Figure 7. First cyclic voltammetry curves recorded at 2 mV/s in sodium acetate (1M) of (a) AD-90°C-1H and AD-70°C-1H and (b) MW-DS at different time and temperature, (c) Evolution of cyclic voltammetry for MW-DS-120°C-30min and (d) Evolution of Q/Q_{max} as a function of the scan rate

By sweeping a larger potential range, between -0.9 V and 0.8 V (*vs.* Ag/AgCl), the reduction from Cu(I) to Cu(0) may occur as underlined before. In the case of MW-DS-120°C-30min, a redox response is observed at low potential (Figure 8a). This redox transformation is related to the Cu(II) to Cu(I) transformation between [-0.2; 0.8] V (*vs.* Ag/AgCl) as indicated by the CVs obtained over the potential range between [-0.2; 0.8] V (*vs.* Ag/AgCl). In the large potential window, the capacity of the CuS electrode is not the same as for the smaller potential range and the two redox reactions take place in cascade. Cu(II) has the possibility to be reduced to Cu(I) and down to Cu(0) at lower potential (-0.9 V *vs.* Ag/AgCl). The transformation of CuS reduced down to Cu(0) explains the differences in intensity and positioning of the redox peaks. Figure 8a compares at the third scan the cycling behaviour of CuS in the two separate potential domains to check the possibility of using the same material at both electrodes.

A full symmetric cell was assembled. Care was taken to equilibrate the capacity in both electrodes, *i.e.*, a loading in mA.h (deduced from half-cell tests) at the negative electrode equivalent to that of the positive electrode. The electrodes were initially cycled in half-cells (two cycles) on their corresponding potential ranges to be passivated and stabilized and then placed face to face in a two-electrodes device. The redox reactions were recorded using linear cyclic voltammetry at 0.2 mV/s (equivalent to a 1.1 C rate of charge or discharge).

The potential of the working electrode was imposed and swept between 0.05 and 0.8 V (*vs.* Ag/AgCl) at a speed of 0.2 mV/s, paying special attention to avoid cell voltage inversion (Fig. 8b and S12). Indeed, a first oxidation at the positive electrode is obtained as the potential is swept between the open circuit potential up to 0.8 V (*vs.* Ag/AgCl) and, simultaneously, the potential at the negative counter-electrode goes down to −0.45 V (*vs.* Ag/AgCl) (Fig. 8b), resulting in a cell voltage of ΔE =

0.8 − (−0.45) = 1.25 V on charge (Fig.8c). The capacity on charge obtained on the first cycle is 48 mA.h/g. By comparison to the half-cell tests, the lower capacity is related to the fact that the potential range chosen is lower and does not enable the entire reduction process to occur, with the discharge of the positive electrode cut at 0.05 V *vs*. Ag/AgCl (ΔE around 0 V) to prevent voltage inversion (Fig S12) since the main reduction of the positive material is centred around 0.1 V. Clearly, the capacity decreases upon cycling at 0.2 mV/s as well as when increasing the scan rate. At a higher scan rate of 50 mV/s, the capacity remains stable but at less than 5 mA.h/g. When the scan rate is slowed down slightly to 2 mV/s, the specific capacity increases moderately to 7 mA.h/g. This indicates that the prepared CuS is not able to sustain high scan rate due to its diffusion-limited redox process, especially in the low potential window corresponding to the activity of the negative electrode (Fig. 7d).

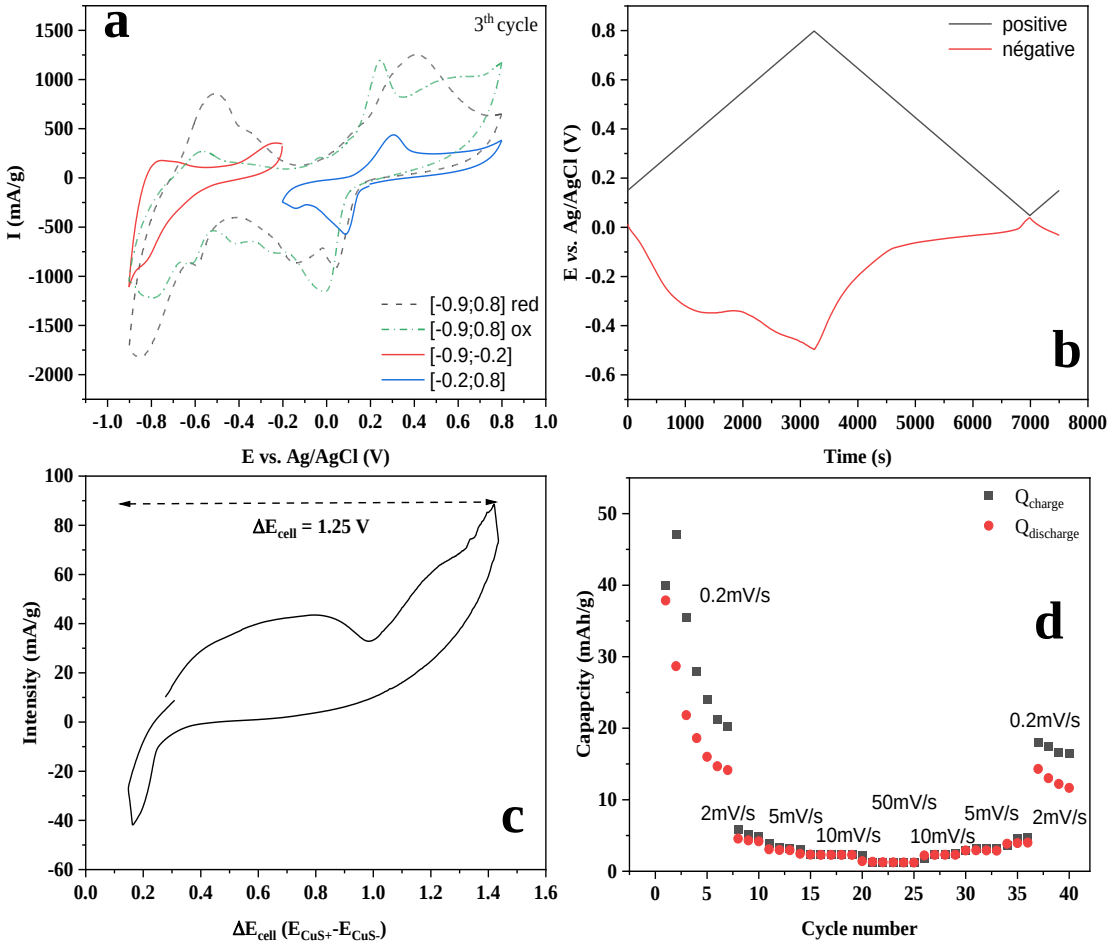

Figure 8. (a) Third cyclic voltammetry curves recorded at 2 mV/s in sodium acetate (1M) of MW-DS-120°C-30 min in different potential range (b) Evolution of CuS positive and CuS negative potential in a complete cell swept between 0.05 and 0.8 V *vs*. Ag/AgCl on the positive working electrode (1M sodium acetate at 0.2 mV/s) (c) Cyclic voltammetry curve of the complete cell (d) Evolution of capacity as a function of the scan rate and number of cycles.

4. Conclusions

In summary, an original approach to synthesize CuS from layered copper hydroxide materials was achieved by applying different protocols. SEM images show particles with a flower-like shape but different in size. Solid state kinetic parameters of the reaction from LSHCu phase yielding CuS are refined by the JMAK method. Refinements indicate a pseudomorphic transformation different in term of precursors phase and protocol applied. The microwave method needs less energy to achieve the transformation than the AD method. When tested in aqueous electrolyte, CuS provides a maximum capacity of 67 mAh/g for the AD and MW-DS-120°C-30min method, which is much higher than for the commercial grade CuS. This is explained by the difference in nanostructuration of the flower-like shape particles obtained from the layered template. Finally, CuS is used as a positive and negative

electrode material in an aqueous battery system, but it is the redox process, which is strongly diffusion limited especially in the lower potential domain, which prevents the whole system from operating at high scan rate (high power).

CRediT authorship contribution statement
All authors: Conceptualization; **J.S** : Formal analysis, Investigation, Writing – original draft ; **F.L**, **C.TG**, **T.B, P.S** : validation, writing review and editing; **P.G**, **G.T**, **C.D** : Validation and Editing

Declaration of competing interest
There are no conflicts of interest to declare.

Data availability
Data will be made available on request.

Acknowledgments
This research was funded by the French Research Agency ANR AAPG2020 "LaDHy", ANR-20-CE05-0024-01. Labex STORE-EX (ANR-10-LABX-76-01) is also acknowledged for financial support.

Supplementary data
Supplementary data to this article can be found online a

References

[1] C. Wang, L. Zhang, Z. Zhang, R. Zhao, D. Zhao, R. Ma, L. Yin, Layered materials for supercapacitors and batteries: Applications and challenges, Progress in Materials Science 118 (2021) 100763. https://doi.org/10.1016/j.pmatsci.2020.100763.
[2] P. Forouzandeh, V. Kumaravel, S.C. Pillai, Electrode Materials for Supercapacitors: A Review of Recent Advances, Catalysts 10 (2020) 969. https://doi.org/10.3390/catal10090969.
[3] X. Peng, L. Peng, C. Wu, Y. Xie, Two dimensional nanomaterials for flexible supercapacitors, Chem. Soc. Rev. 43 (2014) 3303–3323. https://doi.org/10.1039/C3CS60407A.
[4] T. Stimpfling, F. Leroux, Supercapacitor-Type Behavior of Carbon Composite and Replica Obtained from Hybrid Layered Double Hydroxide Active Container, Chem. Mater. 22 (2010) 974–987. https://doi.org/10.1021/cm901860y.
[5] G.M. Tomboc, J. Kim, Y. Wang, Y. Son, J. Li, J.Y. Kim, K. Lee, Hybrid layered double hydroxides as multifunctional nanomaterials for overall water splitting and supercapacitor applications, J. Mater. Chem. A 9 (2021) 4528–4557. https://doi.org/10.1039/D0TA11606H.
[6] K.S. Kumar, N. Choudhary, Y. Jung, J. Thomas, Recent Advances in Two-Dimensional Nanomaterials for Supercapacitor Electrode Applications, ACS Energy Lett. 3 (2018) 482–495. https://doi.org/10.1021/acsenergylett.7b01169.
[7] Y. Zhou, W. Guo, T. Li, A review on transition metal nitrides as electrode materials for supercapacitors, Ceramics International 45 (2019) 21062–21076. https://doi.org/10.1016/j.ceramint.2019.07.151.
[8] S. Mahadik, S. Surendran, J.Y. Kim, G. Janani, D.-K. Lee, T.-H. Kim, J.K. Kim, U. Sim, Syntheses and electronic structure engineering of transition metal nitrides for supercapacitor applications, J. Mater. Chem. A 10 (2022) 14655–14673. https://doi.org/10.1039/D2TA02584A.
[9] J. Li, D. Chen, Q. Wu, Facile synthesis of CoS porous nanoflake for high performance supercapacitor electrode materials, Journal of Energy Storage 23 (2019) 511–514. https://doi.org/10.1016/j.est.2019.03.017.
[10] B. Guan, Y. Li, B. Yin, K. Liu, D. Wang, H. Zhang, C. Cheng, Synthesis of hierarchical NiS microflowers for high performance asymmetric supercapacitor, Chemical Engineering Journal 308 (2017) 1165–1173. https://doi.org/10.1016/j.cej.2016.10.016.
[11] T.-F. Yi, Y. Li, Y.-M. Li, S. Luo, Y.-G. Liu, ZnS nanoparticles as the electrode materials for high-performance supercapacitors, Solid State Ionics 343 (2019) 115074. https://doi.org/10.1016/j.ssi.2019.115074.

[12] Y. Lu, B. Li, S. Zheng, Y. Xu, H. Xue, H. Pang, Syntheses and Energy Storage Applications of MxSy (M = Cu, Ag, Au) and Their Composites: Rechargeable Batteries and Supercapacitors, Advanced Functional Materials 27 (2017) 1703949. https://doi.org/10.1002/adfm.201703949.
[13] J. Barqi, S.M. Masoudpanah, X. Liu, M. Sh. Bafghi, C.K. Ong, Fabrication of porous Cu2S nanosheets for high performance hybrid supercapacitor, Journal of Energy Storage 45 (2022) 103781. https://doi.org/10.1016/j.est.2021.103781.
[14] A. Bahaa, J. Balamurugan, N.H. Kim, J.H. Lee, Metal–organic framework derived hierarchical copper cobalt sulfide nanosheet arrays for high-performance solid-state asymmetric supercapacitors, J. Mater. Chem. A 7 (2019) 8620–8632. https://doi.org/10.1039/C9TA00265K.
[15] X. Shang, J.-Q. Chi, S.-S. Lu, J.-X. Gou, B. Dong, X. Li, Y.-R. Liu, K.-L. Yan, Y.-M. Chai, C.-G. Liu, Carbon fiber cloth supported interwoven WS2 nanosplates with highly enhanced performances for supercapacitors, Applied Surface Science 392 (2017) 708–714. https://doi.org/10.1016/j.apsusc.2016.09.058.
[16] J.-C. Xing, Y.-L. Zhu, Q.-W. Zhou, X.-D. Zheng, Q.-J. Jiao, Fabrication and shape evolution of CoS2 octahedrons for application in supercapacitors, Electrochimica Acta 136 (2014) 550–556. https://doi.org/10.1016/j.electacta.2014.05.118.
[17] J. Theerthagiri, K. Karuppasamy, G. Durai, A.U.H.S. Rana, P. Arunachalam, K. Sangeetha, P. Kuppusami, H.-S. Kim, Recent Advances in Metal Chalcogenides (MX; X = S, Se) Nanostructures for Electrochemical Supercapacitor Applications: A Brief Review, Nanomaterials 8 (2018) 256. https://doi.org/10.3390/nano8040256.
[18] M. Saranya, R. Ramachandran, E.J.J. Samuel, S.K. Jeong, A.N. Grace, Enhanced visible light photocatalytic reduction of organic pollutant and electrochemical properties of CuS catalyst, Powder Technology 279 (2015) 209–220. https://doi.org/10.1016/j.powtec.2015.03.041.
[19] J.-S. Chung, H.-J. Sohn, Electrochemical behaviors of CuS as a cathode material for lithium secondary batteries, Journal of Power Sources 108 (2002) 226–231. https://doi.org/10.1016/S0378-7753(02)00024-1.
[20] Z. Zhao, X. Peng, X. Liu, X. Sun, J. Shi, L. Han, G. Li, J. Luo, Efficient and stable electroreduction of CO2 to CH4 on CuS nanosheet arrays, J. Mater. Chem. A 5 (2017) 20239–20243. https://doi.org/10.1039/C7TA05507B.
[21] T. Dou, Y. Qin, F. Zhang, X. Lei, CuS Nanosheet Arrays for Electrochemical CO2 Reduction with Surface Reconstruction and the Effect on Selective Formation of Formate, ACS Appl. Energy Mater. 4 (2021) 4376–4384. https://doi.org/10.1021/acsaem.0c03190.
[22] M. Mousavi-Kamazani, Z. Zarghami, M. Salavati-Niasari, Facile and Novel Chemical Synthesis, Characterization, and Formation Mechanism of Copper Sulfide (Cu2S, Cu2S/CuS, CuS) Nanostructures for Increasing the Efficiency of Solar Cells, J. Phys. Chem. C 120 (2016) 2096–2108. https://doi.org/10.1021/acs.jpcc.5b11566.
[23] C. Justin Raj, B.C. Kim, W.-J. Cho, W.-G. Lee, Y. Seo, K.-H. Yu, Electrochemical capacitor behavior of copper sulfide (CuS) nanoplatelets, Journal of Alloys and Compounds 586 (2014) 191–196. https://doi.org/10.1016/j.jallcom.2013.10.056.
[24] T. Zhu, B. Xia, L. Zhou, X.W. (David) Lou, Arrays of ultrafine CuS nanoneedles supported on a CNT backbone for application in supercapacitors, J. Mater. Chem. 22 (2012) 7851–7855. https://doi.org/10.1039/C2JM30437F.
[25] K.-J. Huang, J.-Z. Zhang, K. Xing, One-step synthesis of layered CuS/multi-walled carbon nanotube nanocomposites for supercapacitor electrode material with ultrahigh specific capacitance, Electrochimica Acta 149 (2014) 28–33. https://doi.org/10.1016/j.electacta.2014.10.079.
[26] Y.-K. Hsu, Y.-C. Chen, Y.-G. Lin, Synthesis of copper sulfide nanowire arrays for high-performance supercapacitors, Electrochimica Acta 139 (2014) 401–407. https://doi.org/10.1016/j.electacta.2014.06.138.
[27] H. Peng, G. Ma, J. Mu, K. Sun, Z. Lei, Controllable synthesis of CuS with hierarchical structures via a surfactant-free method for high-performance supercapacitors, Materials Letters 122 (2014) 25–28. https://doi.org/10.1016/j.matlet.2014.01.173.
[28] J. Zhang, H. Feng, J. Yang, Q. Qin, H. Fan, C. Wei, W. Zheng, Solvothermal Synthesis of Three-Dimensional Hierarchical CuS Microspheres from a Cu-Based Ionic Liquid Precursor for

High-Performance Asymmetric Supercapacitors, ACS Appl. Mater. Interfaces 7 (2015) 21735–21744. https://doi.org/10.1021/acsami.5b04452.
[29] H. Heydari, S.E. Moosavifard, M. Shahraki, S. Elyasi, Facile synthesis of nanoporous CuS nanospheres for high-performance supercapacitor electrodes, Journal of Energy Chemistry 26 (2017) 762–767. https://doi.org/10.1016/j.jechem.2017.03.007.
[30] B. Pejjai, M. Reddivari, T.R.R. Kotte, Phase controllable synthesis of CuS nanoparticles by chemical co-precipitation method: Effect of copper precursors on the properties of CuS, Materials Chemistry and Physics 239 (2020) 122030. https://doi.org/10.1016/j.matchemphys.2019.122030.
[31] C. Nethravathi, R.N. R., J.T. Rajamathi, M. Rajamathi, Microwave-Assisted Synthesis of Porous Aggregates of CuS Nanoparticles for Sunlight Photocatalysis, ACS Omega 4 (2019) 4825–4831. https://doi.org/10.1021/acsomega.8b03288.
[32] Z. Tian, H. Dou, B. Zhang, W. Fan, X. Wang, Three-dimensional graphene combined with hierarchical CuS for the design of flexible solid-state supercapacitors, Electrochimica Acta 237 (2017) 109–118. https://doi.org/10.1016/j.electacta.2017.03.207.
[33] R. Singhal, D. Thorne, P.K. LeMaire, X. Martinez, C. Zhao, R.K. Gupta, D. Uhl, E. Scanley, C.C. Broadbridge, R.K. Sharma, Synthesis and characterization of CuS, CuS/graphene oxide nanocomposite for supercapacitor applications, AIP Advances 10 (2020) 035307. https://doi.org/10.1063/1.5132713.
[34] T. Zhao, W. Yang, X. Zhao, X. Peng, J. Hu, C. Tang, T. Li, Facile preparation of reduced graphene oxide/copper sulfide composite as electrode materials for supercapacitors with high energy density, Composites Part B: Engineering 150 (2018) 60–67. https://doi.org/10.1016/j.compositesb.2018.05.058.
[35] R. BoopathiRaja, M. Parthibavarman, S. Prabhu, R. Ramesh, A facile one step hydrothermal induced hexagonal shaped CuS/rGO nanocomposites for asymmetric supercapacitors, Materials Today: Proceedings 26 (2020) 3507–3513. https://doi.org/10.1016/j.matpr.2019.06.006.
[36] X. Li, K. Zhou, J. Zhou, J. Shen, M. Ye, CuS nanoplatelets arrays grown on graphene nanosheets as advanced electrode materials for supercapacitor applications, Journal of Materials Science & Technology 34 (2018) 2342–2349. https://doi.org/10.1016/j.jmst.2018.06.013.
[37] K. Jin, M. Zhou, H. Zhao, S. Zhai, F. Ge, Y. Zhao, Z. Cai, Electrodeposited CuS nanosheets on carbonized cotton fabric as flexible supercapacitor electrode for high energy storage, Electrochimica Acta 295 (2019) 668–676. https://doi.org/10.1016/j.electacta.2018.10.182.
[38] W. Zhou, J. Miao, X. Yan, Y. Li, Y. Zhu, W. Zhang, M. Zhang, W. Zhu, M.S. Javed, J. Pan, S. Hussain, Boosted electrochemical performance of CuS anchored on carbon cloth as an integrated electrode for quasi-solid-state flexible supercapacitor, Journal of Electroanalytical Chemistry 897 (2021) 115610. https://doi.org/10.1016/j.jelechem.2021.115610.
[39] K.-J. Huang, J.-Z. Zhang, Y. Liu, Y.-M. Liu, Synthesis of reduced graphene oxide wrapped-copper sulfide hollow spheres as electrode material for supercapacitor, International Journal of Hydrogen Energy 40 (2015) 10158–10167. https://doi.org/10.1016/j.ijhydene.2015.05.152.
[40] H. Peng, G. Ma, K. Sun, J. Mu, H. Wang, Z. Lei, High-performance supercapacitor based on multi-structural CuS@polypyrrole composites prepared by in situ oxidative polymerization, J. Mater. Chem. A 2 (2014) 3303–3307. https://doi.org/10.1039/C3TA13859C.
[41] J. Sarmet, C. Taviot-Gueho, R. Thirouard, F. Leroux, C. Douard, I. Gaalich, T. Brousse, G. Toussaint, P. Stevens, Electrochemical Behavior of Morphology-Controlled Copper (II) Hydroxide Nitrate Nanostructures, Crystal Growth & Design (2023). https://doi.org/10.1021/acs.cgd.2c01468.
[42] M. Ohmasa, M. Suzuki, Y. Takéuchi, A refinement of the crystal structure of covellite, CuS, Mineralogical Journal 8 (1977) 311–319. https://doi.org/10.2465/minerj.8.311.
[43] X. Jiang, Y. Xie, J. Lu, W. He, L. Zhu, Y. Qian, Preparation and phase transformation of nanocrystalline copper sulfides (Cu9S8, Cu7S4 and CuS) at low temperature, J. Mater. Chem. 10 (2000) 2193–2196. https://doi.org/10.1039/b002486o.
[44] C. Li, M. Moliner, A. Corma, Building Zeolites from Precrystallized Units: Nanoscale Architecture, Angewandte Chemie International Edition 57 (2018) 15330–15353. https://doi.org/10.1002/anie.201711422.

[45] A. Galarneau, J. Iapichella, K. Bonhomme, F. Di Renzo, P. Kooyman, O. Terasaki, F. Fajula, Controlling the Morphology of Mesostructured Silicas by Pseudomorphic Transformation: a Route Towards Applications, Advanced Functional Materials 16 (2006) 1657–1667. https://doi.org/10.1002/adfm.200500825.
[46] W.-D. Einicke, H. Uhlig, D. Enke, R. Gläser, Ch. Reichenbach, S.G. Ebbinghaus, Synthesis of hierarchical micro/mesoporous Y-zeolites by pseudomorphic transformation, Colloids and Surfaces A: Physicochemical and Engineering Aspects 437 (2013) 108–112. https://doi.org/10.1016/j.colsurfa.2012.12.024.
[47] L. Liao, K. Zheng, Y. Zhang, X. Li, D. Jiang, J. Liu, Self-templated pseudomorphic transformation of ZIF into layered double hydroxides for improved supercapacitive performance, Journal of Colloid and Interface Science 622 (2022) 309–318. https://doi.org/10.1016/j.jcis.2022.04.088.
[48] J. Joseph, S. Iftekhar, V. Srivastava, Z. Fallah, E.N. Zare, M. Sillanpää, Iron-based metal-organic framework: Synthesis, structure and current technologies for water reclamation with deep insight into framework integrity, Chemosphere 284 (2021) 131171. https://doi.org/10.1016/j.chemosphere.2021.131171.
[49] A. Khawam, D.R. Flanagan, Solid-State Kinetic Models: Basics and Mathematical Fundamentals, J. Phys. Chem. B 110 (2006) 17315–17328. https://doi.org/10.1021/jp062746a.
[50] T. Stimpfling, A. Langry, H. Hintze-Bruening, F. Leroux, In situ platelets formation into aqueous polymer colloids: The topochemical transformation from single to double layered hydroxide (LSH–LDH) uncovered, Journal of Colloid and Interface Science 462 (2016) 260–271. https://doi.org/10.1016/j.jcis.2015.10.010.
[51] D. O'Hare, J.S.O. Evans, A. Fogg, S. O'Brien, Time-resolved, in situ X-ray diffraction studies of intercalation in lamellar hosts, Polyhedron 19 (2000) 297–305. https://doi.org/10.1016/S0277-5387(99)00359-9.
[52] J.S. Blázquez, F.J. Romero, C.F. Conde, A. Conde, A Review of Different Models Derived from Classical Kolmogorov, Johnson and Mehl, and Avrami (KJMA) Theory to Recover Physical Meaning in Solid-State Transformations, Physica Status Solidi (b) 259 (2022) 2100524. https://doi.org/10.1002/pssb.202100524.
[53] K. Shirzad, C. Viney, A critical review on applications of the Avrami equation beyond materials science, Journal of The Royal Society Interface 20 (2023) 20230242. https://doi.org/10.1098/rsif.2023.0242.
[54] E. Haque, C.M. Kim, S.H. Jhung, Facile synthesis of cuprous oxide using ultrasound, microwave and electric heating: effect of heating methods on synthesis kinetics, morphology and yield, CrystEngComm 13 (2011) 4060–4068. https://doi.org/10.1039/C0CE00920B.
[55] G.R. Williams, N.H. Rees, D. O'Hare, Incorporation of phosphorus oxyacids into layered double hydroxides, Solid State Sciences 11 (2009) 1229–1238. https://doi.org/10.1016/j.solidstatesciences.2009.03.019.
[56] N. Mao, C.H. Zhou, D.S. Tong, W.H. Yu, C.X. Cynthia Lin, Exfoliation of layered double hydroxide solids into functional nanosheets, Applied Clay Science 144 (2017) 60–78. https://doi.org/10.1016/j.clay.2017.04.021.
[57] M. Adachi-Pagano, C. Forano, J.-P. Besse, Delamination of layered double hydroxides by use of surfactants, Chem. Commun. (2000) 91–92. https://doi.org/10.1039/A908251D.
[58] Toshiyuki Hibino. Delamination of layered double hydroxides containing amino acids, Chem. Mater. (2004) 16, 25, 5482-5488. https://doi.org/10.1021/cm048842a
[59] B. Huang, W. Wang, T. Pu, J. Li, J. Zhu, C. Zhao, L. Xie, L. Chen, Two-dimensional porous (Co, Ni)-based monometallic hydroxides and bimetallic layered double hydroxides thin sheets with honeycomb-like nanostructure as positive electrode for high-performance hybrid supercapacitors, Journal of Colloid and Interface Science 532 (2018) 630–640. https://doi.org/10.1016/j.jcis.2018.08.019.